



Power Electronic Systems  
Laboratory

© 2012 IEEE

Proceedings of the 38th Annual Conference of the IEEE Industrial Electronics Society (IECON 2012), Montreal, Canada,  
October 25-28, 2012

## The $\eta$ - $\alpha$ -Pareto Front of Inductive Power Transfer Coils

R. Bosshard,  
J. Mühlethaler,  
J. W. Kolar,  
I. Stevanovic

This material is published in order to provide access to research results of the Power Electronic Systems Laboratory / D-ITET / ETH Zurich. Internal or personal use of this material is permitted. However, permission to reprint/republish this material for advertising or promotional purposes or for creating new collective works for resale or redistribution must be obtained from the copyright holder. By choosing to view this document, you agree to all provisions of the copyright laws protecting it.



Eidgenössische Technische Hochschule Zürich  
Swiss Federal Institute of Technology Zurich

# The $\eta$ - $\alpha$ -Pareto Front of Inductive Power Transfer Coils

R. Bosshard\*, J. Mühlethaler\*, J. W. Kolar\*, and I. Stevanović†

\*Power Electronic Systems Laboratory, ETH Zürich, Switzerland, Email: bosshard@lem.ee.ethz.ch

†ABB Switzerland Ltd., Corporate Research, 5405 Baden-Dättwil, Switzerland

**Abstract**—Inductive power transfer (IPT) has been proposed as an alternative charging technology for electric and hybrid electric vehicles (EV/HEV). Because the low magnetic coupling of the transmission coils potentially limits the achievable transmission efficiency  $\eta$ , the losses in the inductors are of key importance in the design of an IPT system. The available area for the receiver coil is usually limited due to the vehicle construction and thus a high area related power density  $\alpha$  of the IPT system is needed. In this paper, it is shown that  $\eta$  is maximized if the resonant compensation is chosen such that only active power is transmitted through the air gap. It is shown that a physical boundary termed the  $\eta$ - $\alpha$ -Pareto front exists, where a trade-off between high efficiency and high area related power density is encountered. A thermal model is used to include the effect of an increased winding temperature into the efficiency calculation. The comparison of the  $\eta$ - $\alpha$ -Pareto fronts of three example designs shows that the shielding of the inductor yields a lower  $\eta$  due to additional losses in the shielding materials and that a higher transmission frequency does not necessarily lead to an efficiency improvement.

## I. INTRODUCTION

The attempt to reduce the global consumption of fossil fuels has promoted the development of electric and hybrid electric vehicles (EV/HEV). Depending on the form of electricity production, they can offer a significantly smaller carbon footprint when compared to traditional vehicles. Moreover, electrical energy as a replacement for traditional fuels leads to reduced operating costs. However, in order to reach a vehicle driving range comparable to that of traditional vehicles (at least 200km), a large battery pack is needed. This not only leads to high initial costs, but also requires a large amount of space on the vehicle and adds additional weight. Recharging the empty battery of an EV/HEV requires up to several hours while refuelling a traditional vehicle is a matter of a few minutes. This is considered a major disadvantage of EV/HEV by many users. With the development of a network of plug-in fast charging stations, recharging times of a few minutes could be achieved. However, fast charging may have a significant impact on battery lifetime as the temperature rise caused by the high charging current as well as the large depth-of-discharge (DOD) lead to faster ageing of the cells [1].

In recent publications, inductive power transmission (IPT) has been proposed for vehicle battery charging [2]–[4]. IPT offers the possibility to recharge the battery without the need for a wired connection. Apart from public recharging stations, this would also allow for recharging units embedded into the road surface at traffic lights, or vehicles could even be recharged whilst driving on a dedicated lane on a highway [5]. Frequent recharging allows reducing the DOD and, depending on the application, also the capacity of the battery could be reduced. This leads to a longer battery lifetime and may enable a reduction of its volume and its cost.

When designing an IPT system for use in an EV/HEV, a number of constructive boundary conditions must be respected. If no additional mechanical or robotic parts for the alignment of the coils are desired, the length of the air gap is given by the construction of the vehicle and the charging station. Typically, an air gap between 100 and 200 mm

must be expected, which leads to a magnetic coupling in the range of 10%-30%. As shown in [6]–[9], the low magnetic coupling directly limits the maximum efficiency  $\eta$  of an inductor. Moreover, in most practical cases the size of the receiver coil is limited to an area of a given size underneath the vehicle. Given the high power level needed to charge an EV/HEV battery, this implies that the area related power density  $\alpha$  of the inductor is of key importance.

Various designs for the inductor coils were proposed [3], [10]–[12]. However, to the knowledge of the authors the relation between the area related power density  $\alpha$  and the efficiency  $\eta$  has not yet been studied. Therefore, in this paper this question is discussed for the IPT system presented in Sec. II. In order to determine the maximum efficiency  $\eta$  given the required area related power density  $\alpha$ , the different possibilities for the resonant compensation of the receiver coil are analyzed in Sec. III. In Sec. IV, an example inductor design as shown in Fig. 1 is optimized at different given receiver radii. A thermal model is included into the calculation to include the effect of an increasing winding temperature. During this process, a boundary termed the  $\eta$ - $\alpha$ -Pareto front which limits the performance of any inductor design is encountered [13]. On the Pareto front, a further increase of one of the performance indices requires a reduction of the other. The  $\eta$ - $\alpha$ -Pareto front is therefore a suitable tool to quantitatively compare the performance of different IPT inductor designs.

Many IPT inductor designs include ferromagnetic or conductive materials to reduce the leakage field in the vicinity of the coils [10], [11]. While the magnetic cores may improve the coupling of the two coils, they add additional weight to the inductor, require more space on the vehicle, and can lead to high core losses at high magnetic field densities or at a high transmission frequency. The conductive shielding materials can lead to eddy current losses and opposing magnetic fields in the air gap that also reduce the efficiency of the system. To the knowledge of the authors, the relation between shielding and efficiency has not yet been analyzed. Therefore, the same optimization is also applied to two example designs that include either ferromagnetic or conductive shielding materials. The obtained results are discussed in Sec. V.

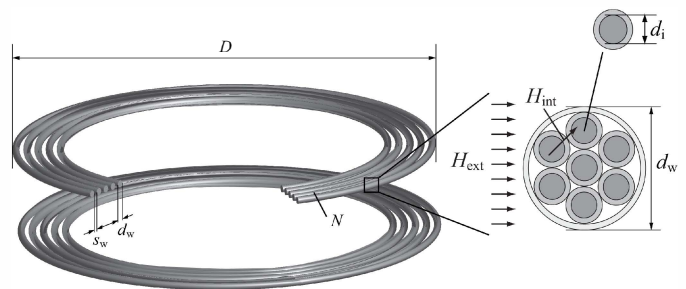


Fig. 1. 3D-Model of one of the analyzed inductor designs (design A).

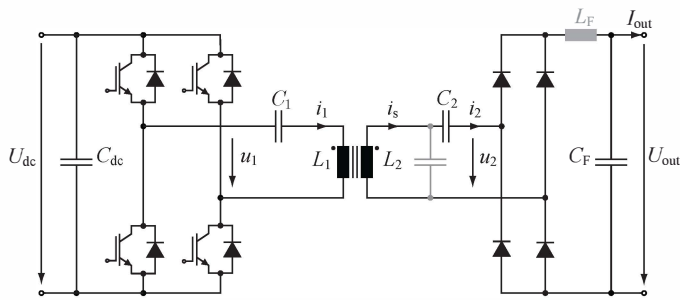


Fig. 2. Overview of the inductive power transfer system. Compensation capacitor  $C_2$  may be connected in series or in parallel to the receiver coil in order to improve the efficiency of the transmission. On the primary side, compensation capacitor  $C_1$  is used to reduce the reactive power that has to be delivered by the voltage source inverter. At the output, a rectifier and an output filter are used to produce a constant output voltage.

## II. INDUCTIVE POWER TRANSFER SYSTEM

In this analysis, an IPT system with specifications typical for an EV/HEV application is investigated. Its nominal parameters are given in Tab. I. Systems of higher power are usually fed from the three-phase grid. Therefore, a dc link voltage of approximately 800 V is typical. Depending on the state-of-charge (SOC), the terminal voltage of an EV/HEV traction battery varies between 400 and 800 V for Li-ion technology. Thus, the output voltage of the system should also be in this range. The transmitted power should be as high as 75 kW to provide a sufficiently fast recharging.

Depending on the construction of the vehicle and the charging station, an air gap between 100 and 200 mm is possible. Due to the resulting low magnetic coupling of the transmission coils, a resonant compensation of the leakage inductance on the transmitter and the receiver side is commonly used to improve the efficiency of the system [7], [9]. As indicated in Fig. 2, the compensation capacitor on the receiver side can either be placed in series or in parallel to the receiver coil. Another capacitor may be connected to the transmitter terminals to reduce the reactive power that has to be supplied by the inverter. Assuming an equal output power, the placement of the primary side capacitor has no influence on the losses in the inductor coils, because the induced voltage on the receiver and the current in the primary coil must remain constant. A series connection of the primary side capacitor allows cancelling the large voltage drop of a transmission coil of high inductance or when operating with a high transmission frequency. Parallel connection of the primary capacitor allows using a higher primary current as only a small part of the current flows through the semiconductors of the inverter. However, owing to the circulating current in the primary resonance tank, the partial load efficiency of such a system is lower [14]. Furthermore, an additional series inductor is required for the connection to a voltage source inverter (VSI). For these reasons, a series connected primary capacitor is used in this work.

To supply the resonant tank, a dc/ac-converter consisting of a voltage link and a full-bridge inverter can be used. The switches are operated with a phase shift modulation as described in [15]. Variation of the duty cycle as well as of the operating frequency allows using zero-current switching (ZCS) at turn-on and turn-off of one bridge-leg, practically freeing it from any switching losses. The other bridge-leg is operated with zero-voltage turn-on and only experiences turn-off losses. For the inverter switches, IGBTs or MOSFETs could be used. With typical IGBT devices, a 2-level topology could be used, while with MOSFETs, a topology with series and parallel connected

TABLE I  
SYSTEM SPECIFICATIONS.

Variable	Value
$U_{dc}$	800 V
$U_{out}$	400 - 800 V
$P_{out}$	0 - 75 kW
$f_0$	20-100 kHz
air gap	100-200 mm

devices is required to carry the large primary current and to block the dc link voltage. Hence, switching frequencies of 20-100 kHz are possible and will be investigated in this paper.

On the secondary side, a diode rectifier and an output filter allow producing the required dc output voltage. Both, a  $LC$ -output filter and a  $C$ -output filter are possible. In order to reduce the weight and volume of the receiver for a given filtering capability, a  $C$ -output filter is preferable [16]. However, it must be ensured that the inductance of the cable connecting the battery to the dc link is sufficient to protect the battery from excessive current ripple. Moreover, the higher stress on the diodes due to oscillations in the diode current resulting from parasitic effects in the inverter is a disadvantage of the  $C$ -output filter. On the other hand, for a  $LC$ -output filter, SiC diodes and possibly a snubber circuit are required to reduce the losses resulting from the hard turn-off of the diodes in the rectifier. The analysis of this trade-off is subject to on-going investigations and will be treated as part of a future work. At this stage, a  $C$ -output filter is assumed.

In order to optimize the IPT system for highest efficiency, the physical limitations on the transmission efficiency at the desired power density  $\alpha$  must be determined. In a first step, a suitable secondary side compensation topology leading to the highest efficiency must be chosen. Therefore, in the next section, the analytical analysis of the circuit shown in Fig. 3a as presented in [9] is extended to the case of a parallel connected compensation capacitor. The results for series and parallel compensation of the receiver are compared and a recommendation for the decision is given.

## III. INDUCTOR LOSS ANALYSIS

In [9], the loss components in the receiver of the resonant circuit shown in Fig. 3a are determined analytically. The results are summarized in the first and second part of this section. A similar analysis can be made for the circuit with a parallel connected compensation capacitor as shown in Fig. 3b. This is presented in the third part of this section. The choice of the primary side compensation capacitor is analyzed in the last part.

### A. Analytical Description of the Resonant Circuit

For both resonant circuits, the definitions given in Tab. II will be used in the analysis. The magnetic coupling of two coils is defined as the ratio of the mutual inductance  $L_h$  and the geometric mean of the two self inductances  $L_1$  and  $L_2$

$$k = \frac{L_h}{\sqrt{L_1 L_2}}. \quad (1)$$

The magnetic coupling strongly depends on the separation of the two coils and typically reaches only values around 10%-30% for IPT systems with an air gap of more than 100 mm.

The primary and secondary quality factors are defined as  $2\pi$  times the ratio of the total stored energy in the circuit and the energy dissipated per period [17]. They can be calculated by

TABLE II  
DEFINITIONS FOR THE ANALYTICAL DESCRIPTION OF THE RESONANT  
CIRCUIT [9].

Definition	Equation
Angular Frequency	$\omega_0 = 2\pi f_0$
Magnetic Coupling	$k = L_h / \sqrt{L_1 L_2}$
Inductance Ratio	$n = \sqrt{L_2 / L_1}$
Transformer Ratio	$\nu = n/k$
Equivalent Load Resistance	$R_L = U_2^2 / P_{\text{out}}$
Matching Factor	$\gamma = R_L / (\omega_0 L_2)$
Capacitance Factor	$\chi = 1 / (\omega_0^2 C_2 L_2)$
Transmitter Quality Factor	$Q_1 = \omega_0 W_{L_1} / P_{\text{loss},1}$
Receiver Quality Factor	$Q_2 = \omega_0 W_{L_2} / P_{\text{loss},2}$
Inductor Quality Factor	$Q = \sqrt{Q_1 Q_2}$
Inductor Quality Ratio	$q = \sqrt{Q_2 / Q_1}$
Transmitter Loss Factor	$\lambda_1 = P_{\text{loss},1} / P_{\text{out}}$
Receiver Loss Factor	$\lambda_2 = P_{\text{loss},2} / P_{\text{out}}$
Total Loss Factor	$\lambda = P_{\text{loss}} / P_{\text{out}}$
Efficiency	$\eta = 1 / (1 + \lambda)$

$$Q_i = 2\pi \frac{W_{L_i}}{P_{\text{loss},i}/f_0} = \frac{1}{2} \frac{\omega_0 L_i \hat{I}_i^2}{P_{\text{loss},i}}, \quad (2)$$

where  $i = 1$  stands for the transmitter and  $i = 2$  for the receiver circuit.  $W_{L_i}$  is the energy stored in the inductor  $L_i$ , and  $P_{\text{loss},i}$  is the respective power loss. If only the dc resistance is considered, (2) can be simplified to

$$Q_i = \frac{\omega_0 L_i}{R_i}. \quad (3)$$

Introducing the equivalent load resistance  $R_L = U_2^2 / P_{\text{out}}$ , which represents the power  $P_{\text{out}}$  delivered to the output at the voltage  $U_2$ , allows defining the matching factor

$$\gamma = \frac{R_L}{\omega_0 L_2}. \quad (4)$$

The matching factor describes how well the resonant circuit is adjusted to the load. The significance of the matching factor will become clear in the following.

To quantify the resonant compensation of the receiver inductance, the capacitance factor is introduced. It is defined as the ratio of the capacitive to the inductive reactance

$$\chi = \frac{X_{C_2}}{X_{L_2}} = \frac{1}{\omega_0^2 C_2 L_2}. \quad (5)$$

For  $\chi = 1$ , the receiver inductance is fully compensated and the reactance values are equal.

### B. Series Compensation of the Receiver

In [9], it is shown that for the circuit with a series compensation capacitor the receiver loss factor can be calculated by

$$\lambda_2 = \frac{P_{\text{loss},2}}{P_{\text{out}}} = \frac{1}{qQ\gamma} \quad (6)$$

and that the calculation of the losses in the primary circuit results in

$$\lambda_1 = \frac{P_{\text{loss},1}}{P_{\text{out}}} = \frac{q}{\gamma Q k^2} \left( \left( \gamma + \frac{1}{qQ} \right)^2 + (1 - \chi)^2 \right). \quad (7)$$

The total inductor loss factor  $\lambda$ , defined as

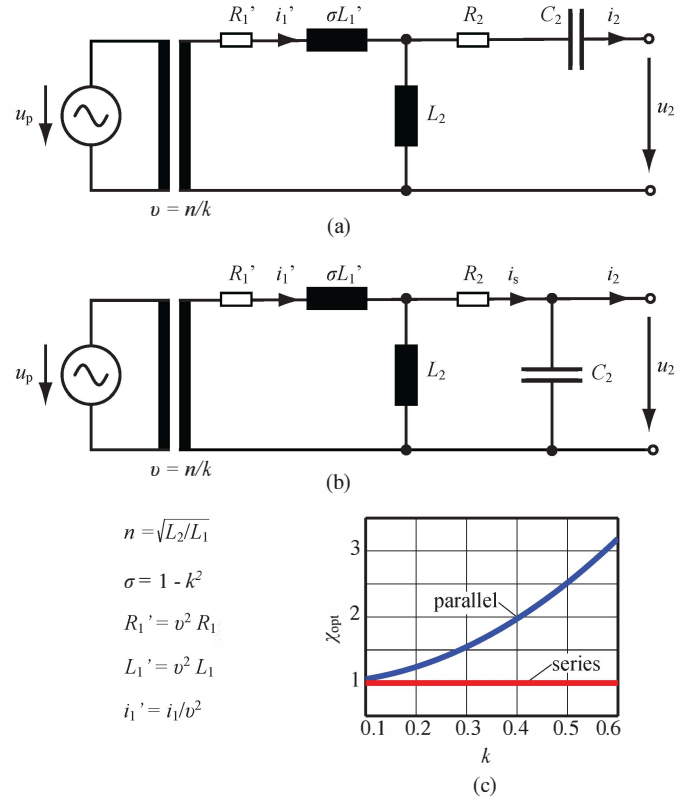


Fig. 3. Equivalent circuit diagram including the inductor and a series connected compensation capacitor (a) or a parallel connected compensation capacitor (b) on the receiver. For the latter case, the optimal capacitance factor  $\chi_{\text{opt}}$  (c) is a function of the magnetic coupling  $k$  and the inductor quality factors ( $Q = 100$  and  $q = 1$ ).

$$\lambda = \lambda_1 + \lambda_2, \quad (8)$$

is minimized for  $\chi_{\text{opt}} = 1$ , independent of the matching factor. This corresponds to the choice

$$C_2 = \frac{1}{\omega_0^2 L_2} \quad (9)$$

for the secondary compensation capacitor. The secondary inductor should be matched to the load according to the optimal matching factor

$$\gamma_{\text{opt}} = \frac{1}{qQ} \sqrt{(kQ)^2 + 1}, \quad (10)$$

where the total loss factor reaches its minimum value of

$$\lambda_{\text{min}} = \frac{2}{(kQ)^2} \left( 1 + \sqrt{1 + (kQ)^2} \right). \quad (11)$$

The corresponding maximum efficiency is

$$\eta_{\text{max}} = \frac{1}{1 + \lambda_{\text{min}}} \approx 1 - \frac{2}{kQ}. \quad (12)$$

As shown by (11), the minimal loss factor is only a function of the factor

$$FOM = kQ. \quad (13)$$

Hence, the factor  $kQ$  is the Figure-of-Merit (*FOM*) for the optimization of an inductor.

### C. Parallel Compensation of the Receiver

A similar derivation can be made for the circuit with a parallel connected compensation capacitor. Using the definitions given in Tab. II, the receiver loss factor can be calculated by

$$\lambda_2 = \frac{1}{qQ\gamma} \left( 1 + \frac{\gamma^2}{\chi^2} \right). \quad (14)$$

Similarly, the transmitter loss factor is found as

$$\lambda_1 = \frac{q}{\gamma Q k^2} \left( \left( \gamma + \frac{1}{qQ} - \frac{\gamma}{\chi} \right)^2 + \left( 1 + \frac{\gamma}{qQ\chi} \right)^2 \right). \quad (15)$$

The total loss factor  $\lambda$  can then be obtained as the sum of (14) and (15). Minimization for a given matching factor  $\gamma$  leads to the optimal capacitance factor

$$\chi_{\text{opt}} = 1 + \frac{1}{(qQ)^2} + \frac{k^2}{q^2}. \quad (16)$$

Note that in this case, the capacitance factor is larger than one. This indicates that more reactive power must be provided by the capacitor than in the case of a series compensation. The values of  $\chi_{\text{opt}}$  are shown in Fig. 3c as a function of the magnetic coupling for an assumed inductor quality factor of  $Q = 100$  and a quality ratio of  $q = 1$ . The minimum of the total loss factor is found at a matching factor of

$$\gamma_{\text{opt}} = \frac{1}{\sqrt{1 + (kQ)^2}} \left( \frac{1}{qQ} + qQ + k^2 \frac{Q}{q} \right). \quad (17)$$

Selecting the optimally matched value of  $L_2$  obtained from (17) and solving (16) for the optimal secondary compensation capacitance leads to [7]

$$C_2 = \frac{1}{2\omega_0^2 L_2} \left( 1 + \sqrt{1 - 4 \left( \frac{\omega_0 L_2}{R_L} \right)^2} \right), \quad (18)$$

and to the resonance frequency

$$\omega_0 = \sqrt{\frac{1}{L_2 C_2} - \frac{1}{(R_L C_2)^2}}. \quad (19)$$

Operation at this point will lead to the minimal loss factor

$$\lambda_{\text{min}} = \frac{2}{(kQ)^2} \left( 1 + \sqrt{1 + (kQ)^2} \right), \quad (20)$$

which is exactly equivalent to (11). Hence, the *FOM* defined in [9] is equally valid for both compensation topologies. Fig. 4a shows the achievable efficiency for both compensation topologies for an inductor with a quality factor of  $Q = 100$ , a quality ratio of  $q = 1$  and three different values of  $k$  in function of the matching factor  $\gamma$ .

An intuitive explanation for the optimality of the solutions shown in this and in the previous section reveals itself when calculating the impedance of the secondary seen from the primary side, often termed the reflected impedance. For both compensation topologies, the reflected impedance has only a real component and thus, only active power is transmitted through the air gap. At this point, the reactive power in the circuit is minimized and hence the efficiency of the system reaches its maximum value.

Note that with the commonly proposed choice  $C_2 = 1/(\omega_0^2 L_2)$  in the case of a parallel compensated secondary, the reflected impedance has also a capacitive component [4] and thus leads to a suboptimal solution in terms of efficiency.

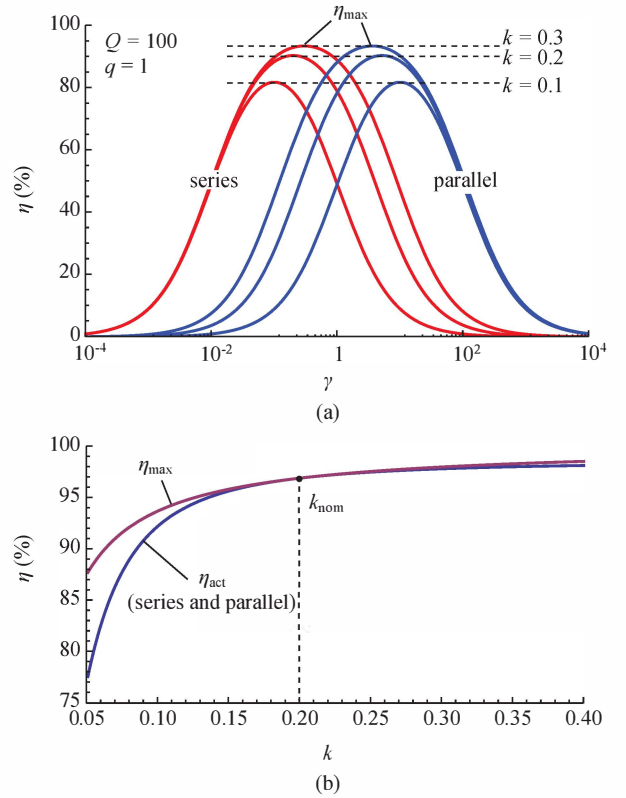


Fig. 4. The maximum efficiency ( $\eta_{\text{max}}$ ) that can be reached with a series or a parallel connected secondary compensation capacitor is exactly equal (a), however, the value  $\gamma_{\text{opt}}$  at which the maximum occurs depends on the chosen compensation topology. Also the efficiency under misalignment ( $\eta_{\text{act}}$ ) is equal for both compensation topologies (b), independent of the value of  $k_{\text{nom}}$  that is used to determine the inductance and capacitance values.

### D. Series Compensation of the Transmitter

In order to reduce the reactive power provided by the dc/ac-converter, another compensation capacitor is added to the primary side of the resonant tank. Because a parallel connection of the primary side compensation capacitor leads to a large reactive current even at low load operation, a series compensation is preferable to obtain a higher partial load efficiency of the system. As the reflected impedance has no reactive part, the value of the primary compensation capacitor is selected to compensate the primary self inductance

$$C_1 = \frac{1}{\omega_0^2 L_1} \quad (21)$$

for both analyzed secondary compensation topologies.

Even though neither the choice of  $C_1$  nor that of  $C_2$  requires a value of  $k$ , a changing magnetic coupling due to misalignment of the coils at a constant load leads to a suboptimal performance. Because the value of  $\gamma_{\text{opt}}$  depends on the magnetic coupling of the coils, coupling variations lead to suboptimal matching of the secondary inductor and thus to a lower efficiency. Choosing a nominal coupling value  $k_{\text{nom}}$  to design the inductor and the capacitors allows calculating the actual efficiency  $\eta_{\text{act}}$  under misalignment. As indicated in Fig. 4b, this value is also equal for both compensation topologies.

In the case of a parallel compensated secondary, a varying load will cause a change of the resonance frequency according to (19). Even though this change can be tracked with an appropriate control

TABLE III  
REQUIRED COMPONENT VALUES AT  $k = 0.3$ ,  $Q = 100$  AND  $q = 1$

	$P_{\text{out}} = 75 \text{ kW}$ , $U_{\text{out}} = 800 \text{ V}$ System		$P_{\text{out}} = 5 \text{ kW}$ , $U_{\text{out}} = 400 \text{ V}$ System	
	Series Compensation	Parallel Compensation	Series Compensation	Parallel Compensation
$f_0$	20 kHz ... 100 kHz	20 kHz ... 100 kHz	20 kHz ... 100 kHz	20 kHz ... 100 kHz
$L_2$	183 $\mu\text{H}$ ... 37 $\mu\text{H}$	15 $\mu\text{H}$ ... 3 $\mu\text{H}$	688 $\mu\text{H}$ ... 138 $\mu\text{H}$	57 $\mu\text{H}$ ... 11 $\mu\text{H}$
$C_2$	345 nF ... 69 nF	3.8 $\mu\text{F}$ ... 767 nF	92 nF ... 18 nF	1 $\mu\text{F}$ ... 205 nF

method, it leads to a detuning of the primary and an increased reactive power demand of the resonant tank and possibly a lower efficiency of the primary side converter. The transmission efficiency, however, will not be affected.

#### IV. INDUCTOR OPTIMIZATION

The presented calculations show that the maximum efficiencies, that can be reached with a series or a parallel connected secondary compensation capacitor, are equal even under misalignment of the coils and depend only on the  $FOM = kQ$ . Therefore, efficiency is no criterion to prefer either of the solutions in the design of an IPT system [7].

A key difference between the two compensation topologies is the value  $\gamma_{\text{opt}}$  at which the maximum occurs [18]. Tab. III shows the required secondary inductor and capacitor values for the IPT system analyzed in this paper as well as for a scaled 5 kW system with an output voltage of only 400 V. It can be seen that the required values of  $L_2$  are much higher for the case of the series connected compensation capacitor. At higher power levels, the size of the coils must be increased to obtain the surface area required for sufficient cooling. With the coil size also the realizable inductance values increase. Therefore, for a high-power IPT system a series compensation topology is preferable as the low inductance value required in the parallel case is hardly realizable. For a low-power IPT system a parallel compensation of the secondary must be chosen as the high inductance values required for a series compensation would lead to an unnecessarily large size of the coils.

In the design of an IPT system for EV/HEV, the size of the receiver coil is limited due to the construction of the vehicle. Hence, it may not always be possible to reach the optimal inductance value. Moreover, if the available area is small, the achievable magnetic coupling is reduced. In the following, a coil optimization based on finite element

(FE) analysis is used to determine the physical limit of the maximum possible efficiency at a given area related power density. Due to the high power level, a series compensation of the receiver is considered in the following.

#### A. Example Designs

In this paper, only axial symmetric designs are considered, but the approach can also be applied to more sophisticated designs. The selected example designs are

- A) Air coils without any shielding or magnetic material
- B) Coils with ferrite shielding planes
- C) Coils with aluminum shielding rings (without ferrite)

The most basic inductor design is to use two planar coils without any core material (A). A common way to improve the magnetic coupling between the inductor coils is to add magnetic core material to both inductors (B). Typically ferrite is used for this purpose. To reduce the leakage flux, aluminum shielding rings can be added to the coils (C) [11]. Fig. 5 shows the results of an FE simulation of the design A.

#### B. Inductor Loss Model

Litz wire is commonly used to reduce the ohmic losses due to the skin and the proximity effect at higher frequencies [19]. An optimal litz wire design has a strand diameter smaller than the skin depth [20], which is  $\delta \approx 0.2 - 0.4 \text{ mm}$  for copper at the frequencies of interest. Hence, a strand diameter of half a skin depth is a feasible choice with available litz wires.

The ohmic losses  $P_{\text{copper}}$  in the wire at the resonant frequency can be determined with the FE tool. For the inductor design using shielding materials, also the core and eddy current losses in the ferrite planes or in the aluminum shield must be taken into account. For

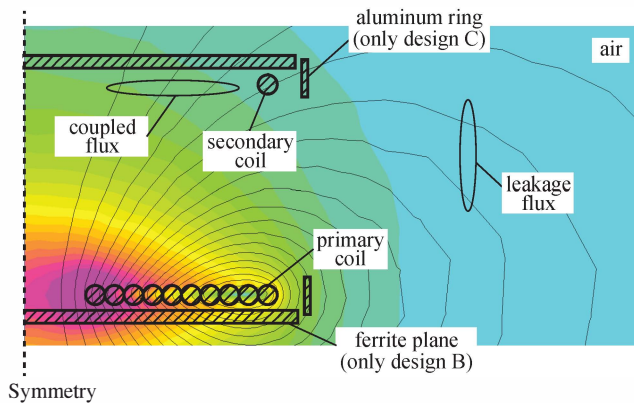


Fig. 5. Example inductor designs: air coils (A), inductor with two ferrite planes (B), and inductor without ferrite plane but with aluminum shielding ring (C).

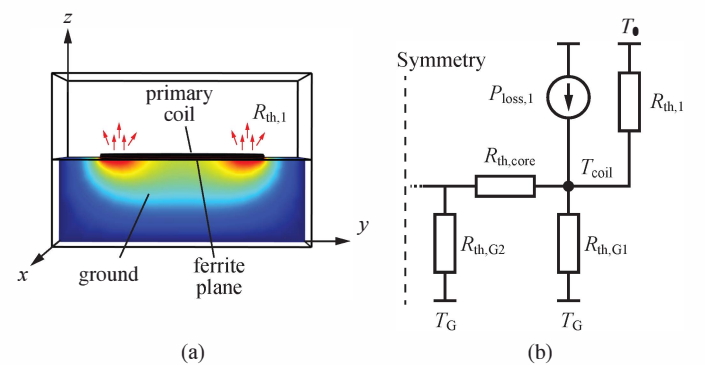


Fig. 6. Results of a thermal simulation of the transmitter coil (a) and thermal circuit diagram (b). A part of the produced heat is dissipated by convection in the air gap, another part is conducted into the ground and along the core material.

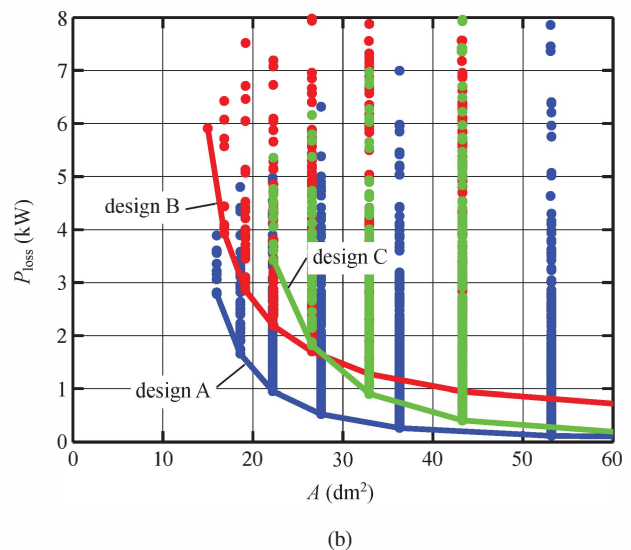
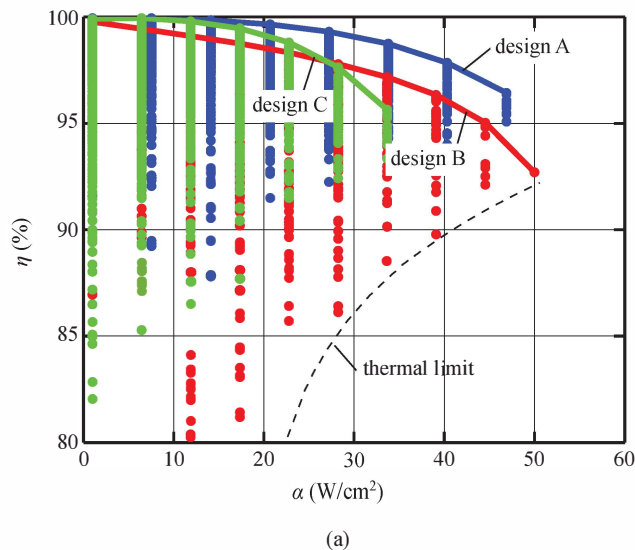


Fig. 7.  $\eta$ - $\alpha$ -Pareto fronts of the three example designs for the transmission of 75 kW through an air gap of 200 mm at 20 kHz (a). Every point is the result of a simulation with a different combination of the design parameters specified in Tab. IV. This implies that a reduction of the loss factor  $\lambda = P_{\text{loss}}/P_{\text{out}}$  requires an increase of the inductor area  $A$  (b).

a sinusoidal excitation, the Steinmetz equation [17] can be used to calculate the power loss per unit volume

$$P'_{\text{core}} = \kappa_{\text{N87}} \cdot f_0^{\alpha_{\text{N87}}} \cdot \hat{B}^{\beta_{\text{N87}}}, \quad (22)$$

where a typical core material, ferrite N87, with the Steinmetz parameters  $\kappa_{\text{N87}} = 1.45$ ,  $\alpha_{\text{N87}} = 1.43$ , and  $\beta_{\text{N87}} = 2.59$  and the conductivity  $\sigma_{\text{N87}} \approx 0 \text{ S/m}$  was chosen. Integrating  $P'_{\text{core}}$  over the core volume leads to the required core losses  $P_{\text{core}}$ . The eddy current losses  $P_{\text{eddy}}$  can also be extracted from the FE tool.

Inserting the total power loss

$$P_{\text{loss},i} = P_{\text{copper},i} + P_{\text{core},i} + P_{\text{eddy},i} \quad (23)$$

into (2) will then allow calculating the quality factors for the transmitter and the receiver.

### C. Thermal Model

The temperature increase of the inductor materials due to the power loss is given by the heat transfer to its environment. As shown in Fig. 6a, one part of the produced heat is dissipated by convection in the air gap while another part is dissipated via conduction into the ground. Fig. 6b shows a thermal circuit diagram of the arrangement. The thermal resistance of the core material is denoted by  $R_{\text{th,core}}$ , the ones of the ground material by  $R_{\text{th,G1}}$  and  $R_{\text{th,G2}}$ . The thermal resistance  $R_{\text{th,1}}$  represents the convective heat transfer into the air gap. The values of the thermal resistances can be determined either with a thermal simulation or with an approximative calculation using empirical values [21].

As all of the loss components presented above depend on temperature, the thermal model must be included into the optimization. In an iterative process, the coil temperature and the losses of the thermal steady-state can be determined. The coil temperature can then be compared to an allowed maximum value as a validity check of the design.

TABLE IV  
PARAMETER SPACE AND LIMIT VALUES FOR THE GEOMETRY OPTIMIZATION OF THE SELECTED EXAMPLE DESIGNS.

Variable	Value
Area related power density	1 ... 100 W/cm <sup>2</sup>
Winding diameter	5 ... 25 mm
Number of turns	1 ... 200
Minimum winding separation	1 mm
Minimum litz wire strand diameter	0.1 mm
Maximum coil temperature	100° C

### D. Implementation

An optimization procedure was implemented to determine the optimal geometry parameters for the example designs introduced above. The geometries were parametrized in terms of inductor diameter  $D$ , winding diameter  $d_w$ , winding separation  $s_w$ , and number of turns  $N_i$ . A minimum separation is required due to the thermal limitation and for the winding insulation. A maximum temperature was chosen according to the heat resistance of typical materials used in the construction of inductors. Tab. IV shows the parameter space and the limiting factors used in the optimization.

All possible parameter combinations are fed to the FE tool, where a field solver is used to determine the magnetic coupling and the inductance values. Based on this information and the optimal capacitance factor  $\chi_{\text{opt}}$  as derived above, the actual currents in the windings can be calculated using the equivalent circuit diagrams shown in Fig. 3. Another simulation with the actual current values is then used to determine the different loss components. The temperature model is used to determine the winding temperature in thermal steady state and update the losses accordingly.

The quality factors for the transmitter and the receiver can be calculated using (2). Using fundamental frequency analysis, the matching factor can be found with [14]

$$\gamma = \frac{R_L}{\omega_0 L_2} \approx \frac{8 U_{\text{out}}^2}{\pi^2 P_{\text{out}} \omega_0 L_2}. \quad (24)$$

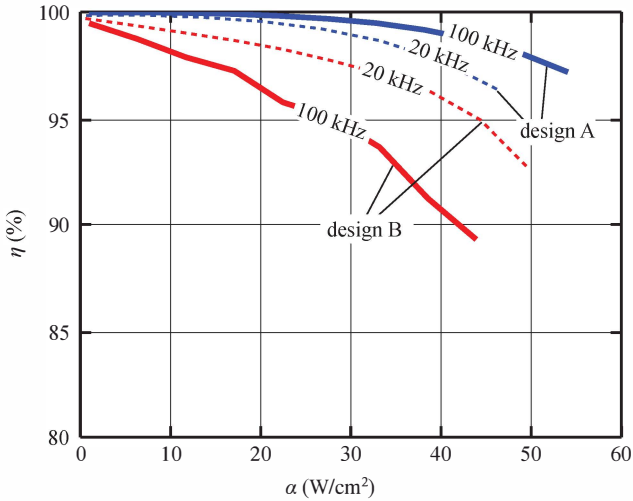


Fig. 8.  $\eta$ - $\alpha$ -Pareto fronts of designs A and B at 100kHz compared to those of 20kHz (also shown in Fig. 7). For design A the higher transmission frequency leads to a higher efficiency, whereas for design B a lower efficiency is observed due to increasing core losses.

Given the *FOM* and the matching factor, the total loss factor of the design can then be found using (8). Its efficiency follows as  $\eta = 1/(1 + \lambda)$ .

## V. RESULTS

### A. $\eta$ - $\alpha$ -Pareto Front

The results of the parameter sweep are shown in Fig. 7a. Every point represents a design with a different combination of the design parameters specified in Tab. IV. It is clearly visible, that a maximum efficiency exists for each value of the area related power density  $\alpha$ . This performance boundary, termed the  $\eta$ - $\alpha$ -Pareto front, represents the physical performance limits of the three example designs. Fig. 7b shows the same results in a plot of the actual inductor area versus the power loss.

These results indicate that with a sufficiently large inductor, a very high transmission efficiency can be achieved. However, if the available space for the inductor is limited and, therefore, a high area related power density is required, only a reduced efficiency can be achieved.

### B. Influence of the Transmission Frequency

Fig. 8 shows the  $\eta$ - $\alpha$ -Pareto fronts of designs A and B at the frequencies 20 and 100 kHz. The comparison shows that for design A without shielding, the higher transmission frequency leads to a higher efficiency due to the increased quality factor. However, for design B that includes a magnetic core, the coil quality decreases due to higher core losses. This implies that even though it reduces the required primary current, an increase of the transmission frequency does not automatically improve the design. However, to be able to compare the overall performance of the design at different frequencies, the physical properties of the switches (IGBT at 20kHz or MOSFET at 100kHz) as well as the switching losses resulting from the modulation scheme have to be included in the calculation of the efficiency.

### C. Effect of Shielding

A similar effect can also be observed if the effectiveness of the shielding is analyzed. As shown in Fig. 9, the ferrite planes

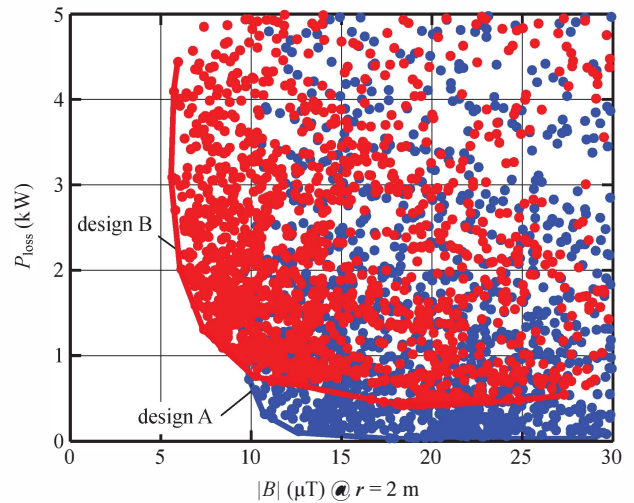


Fig. 9. Magnetic flux density at a point 2 m away from the coil center, shown for designs A and B. A reduction of the leakage flux is only feasible with a less efficient design.

used in design B allow reducing the leakage flux density. However, the reduction leads to a lower efficiency as the inductor quality is decreased due to the additional core losses. A good measure for the performance of an inductor in this respect is the leakage field attenuation  $\beta$ , which shall be defined as the ratio between the maximum allowed magnetic flux density and the actual magnetic flux density at a certain distance from the coil center<sup>1</sup>  $\beta = B_{\max}/B_{\text{act}}$ . More analysis of the relation of the parameter  $\beta$  and the efficiency will be part of a future publication.

## VI. CONCLUSION

For the design of an IPT inductor under the boundary conditions encountered in applications with EV/HEV, the inductor coils are optimized for efficiency  $\eta$  and area related power density  $\alpha$ . It was shown that the maximum efficiency with a series or a parallel compensation of the receiver are equal if the capacitor is chosen such that only active power is transmitted through the air gap. Hence, efficiency is no criterion for the choice of a compensation topology. However, the size required to provide sufficient surface area for the cooling of the coils limits the possible secondary inductance values and gives an indication for an optimal choice of the compensation topology. A physical boundary termed the  $\eta$ - $\alpha$ -Pareto front, where an improvement of one of the performance indices requires the reduction of the other is encountered. The  $\eta$ - $\alpha$ -Pareto front is therefore a suitable tool to quantitatively compare the performance of different IPT inductor designs. Using the  $\eta$ - $\alpha$ -Pareto, it was shown that depending on the coil materials used in the design, a higher transmission frequency can lead to an increase or a decrease of the transmission efficiency. For two example designs that include ferrite or aluminum shielding materials, it was shown that a reduction of the leakage flux in the vicinity of the coils is only possible if additional transmission losses are accepted.

## ACKNOWLEDGMENT

The authors would like to thank ABB Switzerland Ltd. for their funding and for their support regarding many aspects of this research project.

<sup>1</sup>The measurement distance was chosen as  $r = 2$  m in Fig. 9.

## REFERENCES

- [1] D. Magnor, J. B. Gerschler, M. Ecker, P. Merk, and D. U. Sauer, "Concept of a battery aging model for lithium-ion batteries considering the lifetime dependency on the operation strategy," *Proc. of the 24th European Photovoltaic Solar Energy Conference*, 2009.
- [2] R. M. Miskiewicz, A. J. Moradewicz, and M. P. Kazmierkowski, "Contactless battery charger with bi-directional energy transfer for plug-in vehicles with vehicle-to-grid capability," in *Proc. of the IEEE Int. Industrial Electronics (ISIE) Symp.*, 2011, pp. 1969–1973.
- [3] A. L. Jesús Sallán, Juan L. Villa and J. F. Sanz, "Optimal design of ICPT systems applied to electric vehicle battery charge," *IEEE Transactions on Industrial Electronics*, vol. 56, no. 6, pp. 2140–2149, 2009.
- [4] C.-S. Wang, O. H. Stielau, and G. A. Covic, "Design considerations for a contactless electric vehicle battery charger," *IEEE Transactions on Industrial Electronics*, vol. 52, no. 5, pp. 1308–1314, 2005.
- [5] M. Budhia, G. Covic, and J. Boys, "Magnetic design of a three-phase inductive power transfer system for roadway powered electric vehicles," *Proc. of the IEEE Vehicle Power and Propulsion Conf. (VPPC)*, pp. 1–6, 2010.
- [6] J. C. Schuder, "Powering an artificial heart: Birth and of the inductively and coupled-radio frequency system in 1960," *Artificial Organs*, vol. 26, no. 11, pp. 909–915, 2002.
- [7] K. Van Schuylenbergh and R. Puers, *Inductive Powering: Basic Theory and Application to Biomedical Systems*, 1st ed. Springer Science, 2009.
- [8] B. Lenaerts and R. Puers, *Omnidirectional Inductive Powering for Biomedical Implants*, 1st ed. Springer Science, 2009.
- [9] E. Waffenschmidt and T. Staring, "Limitation of inductive power transfer for consumer applications," in *Proc. of the 13th European Conf. Power Electronics and Applications (EPE)*, 2009, pp. 1–10.
- [10] M. Budhia, J. Boys, G. Covic, and C. Huang, "Development of a single-sided flux magnetic coupler for electric vehicle IPT charging systems," *IEEE Transactions on Industrial Electronics*, 2011, early access.
- [11] M. Budhia, G. A. Covic, and J. T. Boys, "Design and optimization of circular magnetic structures for lumped inductive power transfer systems," *IEEE Transactions on Power Electronics*, vol. 26, no. 11, pp. 3096–3108, 2011.
- [12] R. D. L. Seung-Hwan Lee, "A design methodology for multi-kW, large airgap, MHz frequency, wireless power transfer systems," *Proc. of the IEEE Energy Conversion Congress and Exposition (ECCE)*, pp. 3503 – 3510, 2011.
- [13] T. M. Andersen, C. M. Zingerli, F. Krismer, J. W. Kolar, and C. O'Mathuna, "Inductor optimization procedure for power supply in package and power supply on chip," in *Proc. of the IEEE Energy Conversion Congress and Exposition (ECCE)*, 2011, pp. 1320–1327.
- [14] R. L. Steigerwald, "A comparison of half-bridge resonant converter topologies," *IEEE Transactions on Power Electronics*, vol. 3, no. 2, pp. 174–182, April 1988.
- [15] F. da Silveira Cavalcante, "High output voltage series-parallel resonant dc-dc converter for medical x-ray imaging applications," Ph.D. dissertation, Swiss Federal Institute of Technology Zurich (ETHZ), 2006.
- [16] J. Biela, U. Badstuebner, and J. W. Kolar, "Design of a 5-kW, 1-U, 10-kW/dm<sup>3</sup> resonant dc-dc converter for telecom applications," *IEEE Transactions on Power Electronics*, vol. 24, no. 7, pp. 1701–1710, 2009.
- [17] R. W. Erickson and D. Maksimovic, *Fundamentals of Power Electronics*, 2nd ed. Springer Science, 2001.
- [18] G. Vandevoorde and R. Puers, "Wireless energy transfer for stand-alone systems: A comparison between low and high power applicability," *Sensors a*, vol. 92, no. 1-3, pp. 305–311, 2000.
- [19] J. Mühlethaler, J. W. Kolar, and A. Ecklebe, "Loss modeling of inductive components employed in power electronic systems," in *Proc. of the 8th IEEE Int. Power Electronics and ECCE Asia (ICPE & ECCE) Conf.*, 2011, pp. 945–952.
- [20] C. R. Sullivan, "Optimal choice for number of strands in a litz-wire transformer winding," *IEEE Transactions on Power Electronics*, vol. 14, no. 2, pp. 283–291, Dec. 1999.
- [21] *VDI Heat Atlas*, 2nd ed. Springer-Verlag, Berlin, 2010.